

Supplementary Information: Mechanism of magnetization reduction in iron oxide nanoparticles

Tobias Köhler,^{*a,b,c} Artem Feoktystov,^a Oleg Petravic,^b Emmanuel Kentzinger,^b Tanvi Bhatnagar-Schöffmann,^{b,c,d} Mikhail Feygenson,^e Nileena Nandakumaran,^{b,c} Joachim Landers,^f Heiko Wende,^f Antonio Cervellino,^g Ulrich Rücker,^b András Kovács,^d Rafal E. Dunin-Borkowski,^d and Thomas Brückel^{b,c}

^a Forschungszentrum Jülich GmbH, Jülich Centre for Neutron Science JCNS at Heinz Maier-Leibnitz Zentrum MLZ, 85748 Garching, Germany.

^b Forschungszentrum Jülich GmbH, Jülich Centre for Neutron Science JCNS-2 and Peter Grünberg Institute PGI-4, JARA-FIT, 52425 Jülich, Germany.

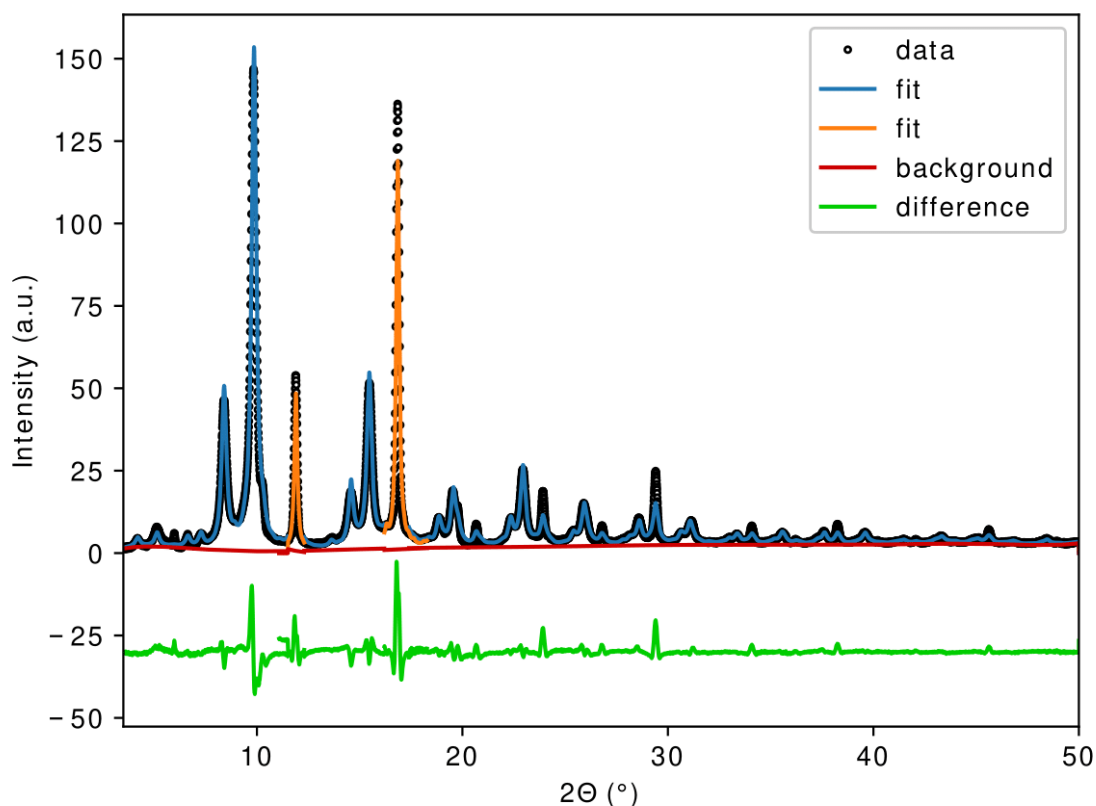
^c Lehrstuhl für Experimentalphysik IV C, RWTH Aachen University, 52056 Aachen, Germany.

^d Forschungszentrum Jülich GmbH, Ernst Ruska-Centre for Microscopy and Spectroscopy with Electrons and Peter Grünberg Institute, 52425 Jülich, Germany.

^e Jülich Centre for Neutron Science (JCNS-1) and Institute for Complex Systems (ICS-1), Forschungszentrum Jülich GmbH, 52425 Jülich, Germany

^f Faculty of Physics and Center for Nanointegration Duisburg-Essen (CENIDE), University of Duisburg-Essen, 47057 Duisburg, Germany.

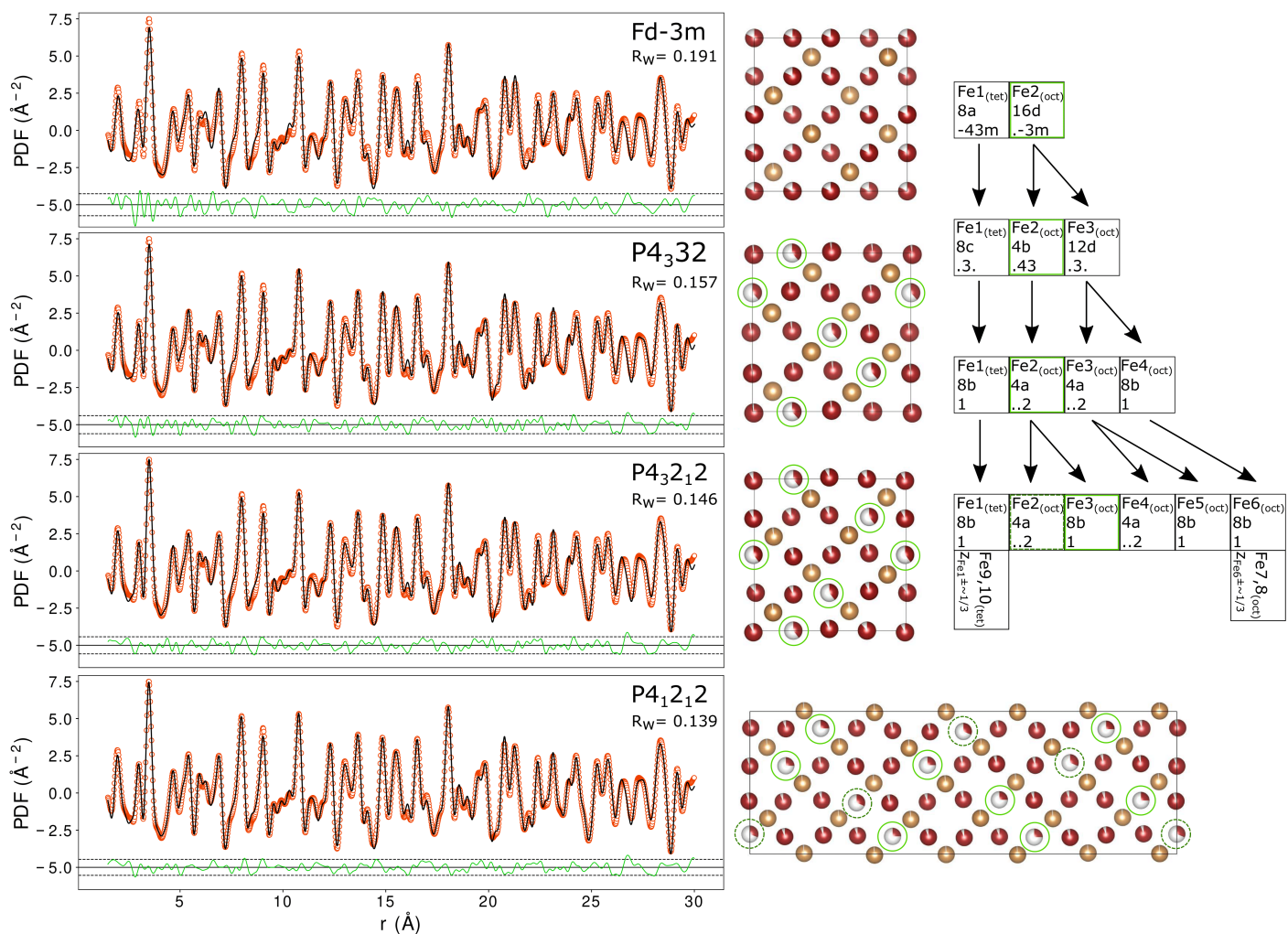
^g Paul Scherrer Institut, Swiss Light Source, 5232 Villigen PSI, Switzerland.



Supplementary Figure S1 Rietveld refinement of the powder XRD data with spacegroup model $P4_32_12$ and parameters listed in tab S1. For peaks (400) and (440) (orange lines) only the coherent crystallite size was changed.

Supplementary crystal structure and PDF analysis discussion

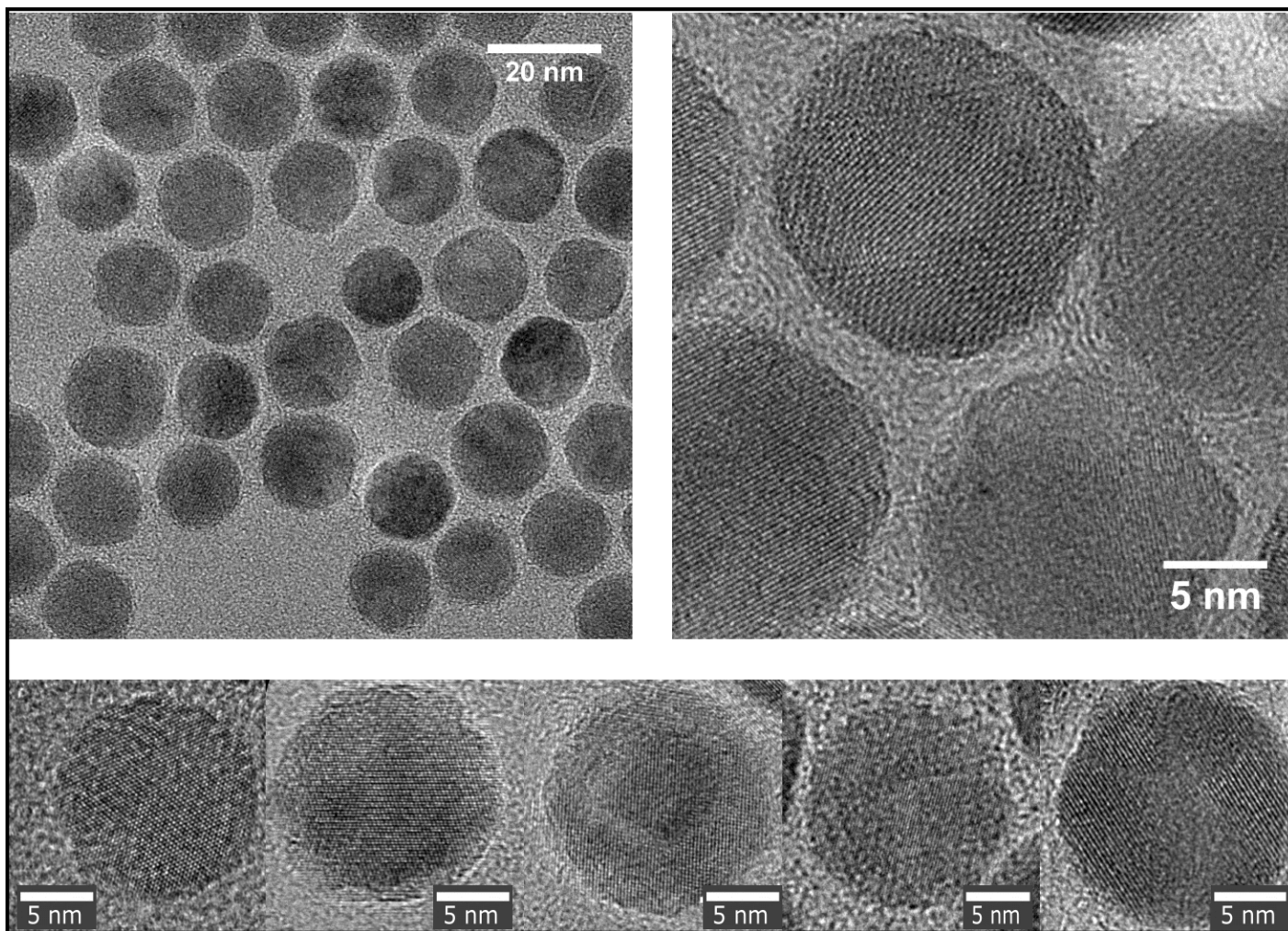
To determine the crystal structure of the nanoparticles and to address the question of possible vacancy ordering refinements on the PDF data were performed systematically with decreasing symmetry spacegroups associated with increased vacancy ordering. Kelm et al.¹ constructed a continuous group-subgroup relation between disordered cubic maghemite/magnetite with the spacegroup Fd-3m down to the tetragonal structure with symmetry $P4_12_12$. A continuous change of the crystal symmetry and therefore unbroken chain of group-subgroup relations is expected for a continuous transition from magnetite to maghemite, which is also confirmed by the continuous transition of the respective lattice parameters as observed by². Group theoretical considerations leave only the group-subgroup chain of Fd-3m - $F4_132$ - $P4_332$ ($P4_132$) - $P4_32_12$ ($P4_12_12$) - $P4_12_12$ ($P4_32_12$). The last step involves a tripling of the unit cell along the c direction. In parentheses are the enantiomorphic space groups, that differ only in the handedness of the screw axis. The cubic structure with spacegroup Fd-3m contains only two independent iron positions, for tetrahedral and octahedral iron. The octahedral iron position is then split into an increasing number of independent positions due to the decrease in symmetry (fig. S2). This results also in an increase of the refinement parameters from 17 for Fd-3m to 80 for $P4_12_12$ with a tripled unit cell. Fits to the PDF in a r-range of 1.5 to 30 Å show an improvement of the fit quality with the lower symmetry space groups. The best fits are obtained with the tetragonal space groups $P4_32_12$ and $P4_12_12$. However, the $P4_32_12$ fit reaches a R_w value of 0.146 with 33 independent parameters, while for $P4_12_12$ with a tripled unit cell R_w is 0.139 with 80 parameters. This small increase in fit quality with more than twice as many parameters suggests that the higher symmetry space group $P4_32_12$ is sufficient to describe the structure and any remaining discrepancies between the model and the data are most likely due to structural disorder in the crystallites that can not be captured with the small-box modelling approach used in PDFGui. In a comparison of the R_w -values for a fit range of 1.5 to 10 Å this becomes even clearer (tab.S1). Here the cubic inverse spinel structure Fd-3m is not able to describe the local structure leading to $R_w = 0.211$. The difference in fit quality for the tetragonal structures is even smaller for this fit range, further suggesting to use the $P4_32_12$ structure that requires less parameters. A Rietveld refinement of the powder XRD-pattern with the structure obtained from the PDF-analysis shows that all features are reasonably well reproduced, including the superstructure peaks at low angles (Fig S1). Based on the assumption of larger coherent crystallite size in the directions perpendicular to the lattice planes (400) and (440) the particle size parameter was changed for those peaks (orange in Fig S1) resulting in a sharper peak profile and a better fit.



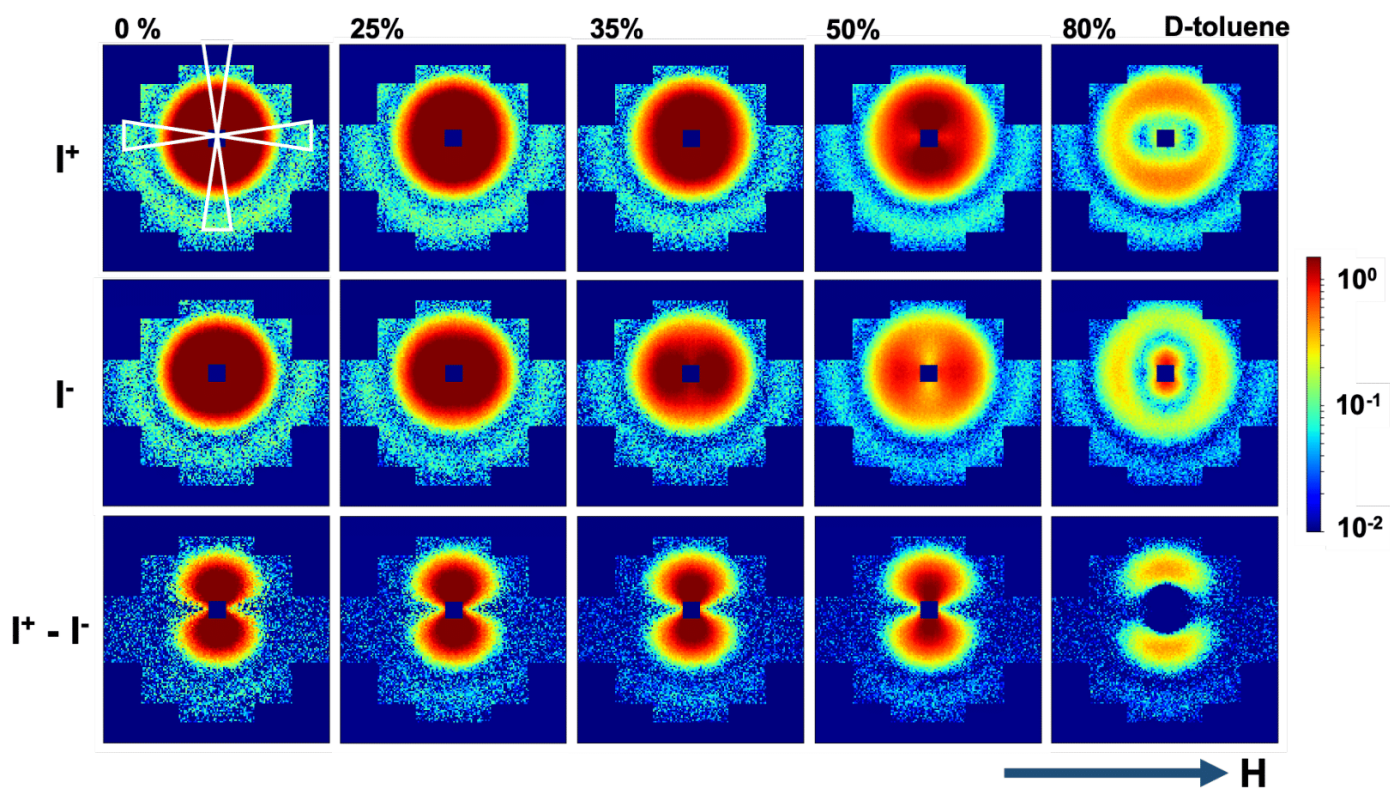
Supplementary Figure S2 Best fits for the 4 different structural models, representing an increase of vacancy ordering and a subsequent decrease of crystal symmetry. The group-subgroup relationships and the splitting of the iron sites due to the change in symmetry are shown on the right (after¹). Structural models are also shown with red balls representing octahedral iron positions and yellow balls showing tetrahedrally coordinated iron. Vacancy positions are indicated with partially filling of the balls and in case of ordering the respective sites are marked with green circles. The splitting of the iron positions with decreasing symmetry is shown on the right. The positions where a majority of vacancies is expected are marked with green.

Supplementary Table S1 PDF analysis results with four different starting models (see fig.S2). For all structures only isotropic displacements were refined and the Uiso factors of all oxygen atoms were constrained to one value. For the tetragonal structure with a tripled unit cell (P4₁2₁2) only one site occupancy factor (SOF) was refined for tetrahedral atoms and the SOF of octahedral positions Fe5-Fe8 were also constrained, leaving only Fe2 and Fe3 independent as vacancies are likely to form on these sites (see fig.S2 for the group-subgroup relationships).

Spacegroup	Position	Mult.	x/a	y/b	z/c	Uiso	SOF	
Fd-3m	Fe1(tet.)	8	0.125	0.125	0.125	0.0068(5)	0.98(2)	
	Fe2(oct.)	16	0.5	0.5	0.5	0.0158(5)	0.83(2)	
	O1	32	0.2549(5)	0.2549(5)	0.2549(5)	0.0144(5)	1	
	a=b=c ()	8.357(2)						
	δ (°)	1.18(1)						
	Particle size ()	107(5)						
	Parameters	10						
	R _w	0.191	(R _w 1.5-10 Å	0.211)				
	<hr/>							
	P4 ₃ 32	Fe1(tet.)	8	0.9973(5)	0.9973(5)	0.9973(5)	0.0062(5)	1.0(2)
Fe2(oct.)		4	0.625	0.625	0.625	0.0130(5)	0.39(2)	
Fe3(oct.)		12	0.3663(5)	0.8837(5)	0.125	0.0073(5)	0.97(2)	
O1		8	0.3817(5)	0.3817(5)	0.3817(5)	0.0144(5)	1	
O2		24	0.6229(5)	0.1168(5)	0.8795(5)	0.0144(5)	1	
a=b=c ()		8.358(2)						
δ (°)		1.34(1)						
Particle size ()		104(5)						
Parameters		17						
R _w		0.157	(R _w 1.5-10 Å	0.151)				
<hr/>								
P4 ₃ 2 ₁ 2	Fe1(tet.)	8	0.7469(5)	0.9985(5)	0.1201(5)	0.0068(5)	0.98(2)	
	Fe2(oct.)	4	0.3672(5)	0.6328(5)	0.75	0.0073(5)	0.39(2)	
	Fe3(oct.)	4	0.1205(5)	0.8795(5)	0.25	0.0069(5)	0.93(2)	
	Fe4(oct.)	8	0.3685(5)	0.8683(5)	0.9866(5)	0.0067(5)	0.92(2)	
	O1	8	0.1414(5)	0.3833(5)	0.5077(5)	0.0119(5)	1	
	O2	8	0.3794(5)	0.1314(5)	0.0013(5)	0.0119(5)	1	
	O3	8	0.1299(5)	0.8676(5)	0.0232(5)	0.0119(5)	1	
	O4	8	0.3749(5)	0.6293(5)	0.9933(5)	0.0119(5)	1	
	a=b ()	8.358(2)						
	c	8.358(2)						
δ (°)	1.66(1)							
Particle size ()	106(5)							
Parameters	33							
R _w	0.146	(R _w 1.5-10 Å	0.128)					
<hr/>								
P4 ₁ 2 ₁ 2	Fe1(tet.)	8	0.7485(5)	0.0315(5)	0.0402(5)	0.0068(5)	0.98(2)	
	Fe2(oct.)	4	0.3599(5)	0.6401(5)	0.25	0.1042(5)	0.31(2)	
	Fe3(oct.)	8	0.6190(5)	0.3759(5)	0.0842(5)	0.0053(5)	0.25(2)	
	Fe4(oct.)	4	0.6168(5)	0.6168(5)	0	0.0055(5)	0.94(2)	
	Fe5(oct.)	8	0.1222(5)	0.8807(5)	0.0817(5)	0.0065(5)	0.94(2)	
	Fe6(oct.)	8	0.3712(5)	0.8847(5)	0.9980(5)	0.0046(5)	0.94(2)	
	Fe7(oct.)	8	0.3580(5)	0.8675(5)	0.3278(5)	0.0052(5)	0.94(2)	
	Fe8(oct.)	8	0.3780(5)	0.8662(5)	0.6656(5)	0.0079(5)	0.94(2)	
	Fe9(tet.)	8	0.7503(5)	0.9927(5)	0.7080(5)	0.0068(5)	0.98(2)	
	Fe10(tet.)	8	0.7431(5)	0.9953(5)	0.3730(5)	0.0068(5)	0.98(2)	
	O1	8	0.1373(5)	0.3634(5)	0.1748(5)	0.0092(5)	1	
	O2	8	0.1305(5)	0.3773(5)	0.5053(5)	0.0092(5)	1	
	O3	8	0.1307(5)	0.3880(5)	0.8357(5)	0.0092(5)	1	
	O4	8	0.3641(5)	0.1154(5)	0.0004(5)	0.0092(5)	1	
	O5	8	0.3854(5)	0.1097(5)	0.3338(5)	0.0092(5)	1	
	O6	8	0.3730(5)	0.1338(5)	0.6672(5)	0.0092(5)	1	
	O7	8	0.1258(5)	0.8851(5)	0.0012(5)	0.0092(5)	1	
	O8	8	0.1320(5)	0.8790(5)	0.3380(5)	0.0092(5)	1	
	O9	8	0.1277(5)	0.8795(5)	0.6700(5)	0.0092(5)	1	
	O10	8	0.3440(5)	0.6170(5)	0.0026(5)	0.0092(5)	1	
O11	8	0.3695(5)	0.6288(5)	0.3280(5)	0.0092(5)	1		
O12	8	0.3675(5)	0.6317(5)	0.6703(5)	0.0092(5)	1		
a=b ()	8.358(2)							
c	25.073(2)							
δ (°)	1.79(1)							
Particle size ()	108(5)							
Parameters	80							
R _w	0.139	(R _w 1.5-10 Å	0.124)					



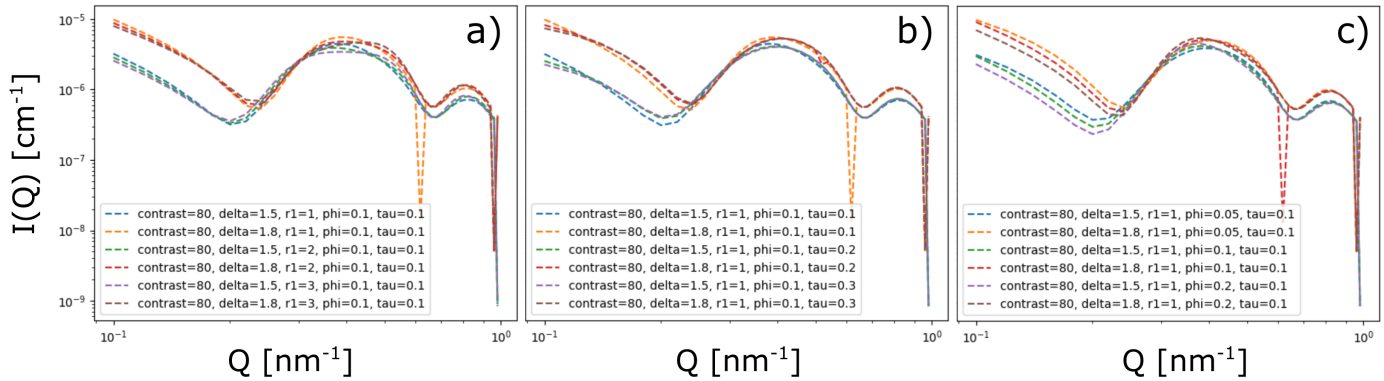
Supplementary Figure S3 Bright field TEM micrographs showing particles in different orientations to the electron beam resulting in varying lattice fringes and contrasts.



Supplementary Figure S4 Detector images recorded at KWS-1 with a sample to detector distance of 2 m. Columns show increasing deuteration of the solvent from 0% D-toluene to 80%. The rows are from top to bottom the spin-up channel, the spin-down channel and the difference between up and down, i.e. the nuclear-magnetic interference term. The field of 0.5 T was applied horizontally indicated by the blue arrow. In the first detector image the sectors that were used for averaging are indicated with white lines. All plots are on a logarithmic scale.

Supplementary Table S2 Results of the inductively coupled plasma optical emission spectroscopy (ICP-OES).

Sample		Mean	standard deviation
Total	mg	33.35	-
Co	$\mu\text{g}/\text{sample}$	<0.01	-
Fe	$\mu\text{g}/\text{sample}$	1.363	0.017
Ni	$\mu\text{g}/\text{sample}$	<0.03	-
Gd	$\mu\text{g}/\text{sample}$	<0.06	-
Cr	$\mu\text{g}/\text{sample}$	<0.001	-
Al	$\mu\text{g}/\text{sample}$	0.7	0.03

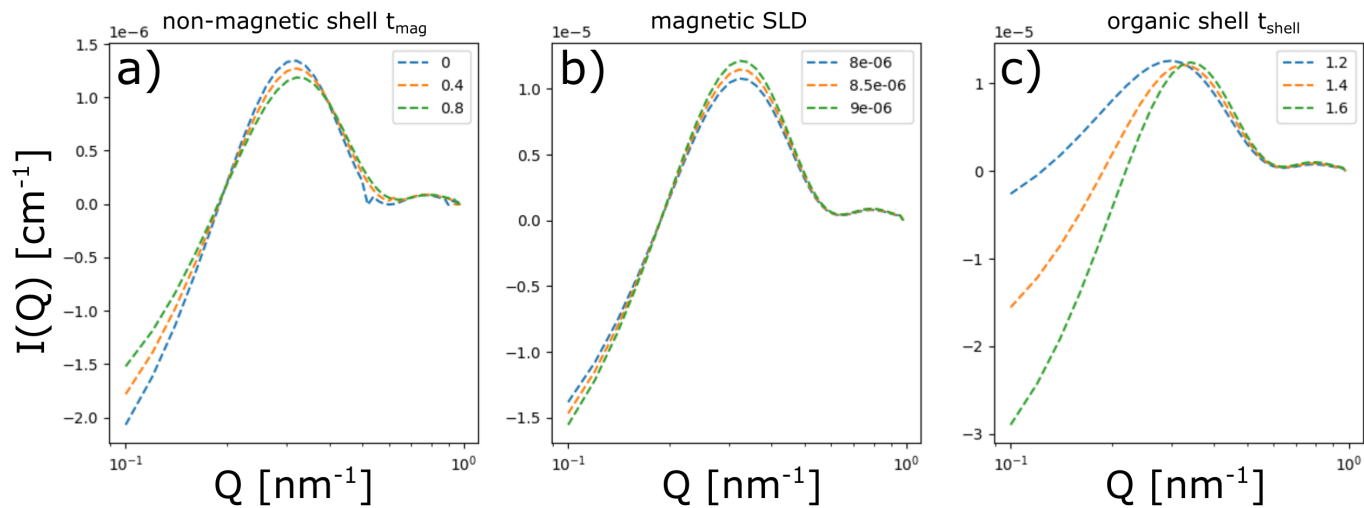
**Supplementary Figure S5** Simulated scattering curves parallel to an applied field, i.e. the nuclear formfactor and the influence of particle interactions via a sticky hard sphere structure factor. a) Variations in organic shell thickness (delta) and volume fraction parameter phi. b) Variation of delta and stickiness parameter tau. c) Variation of delta and a small addition to the total radius, $r1$, giving an effective radius.

Details of the small angle neutron scattering data analysis

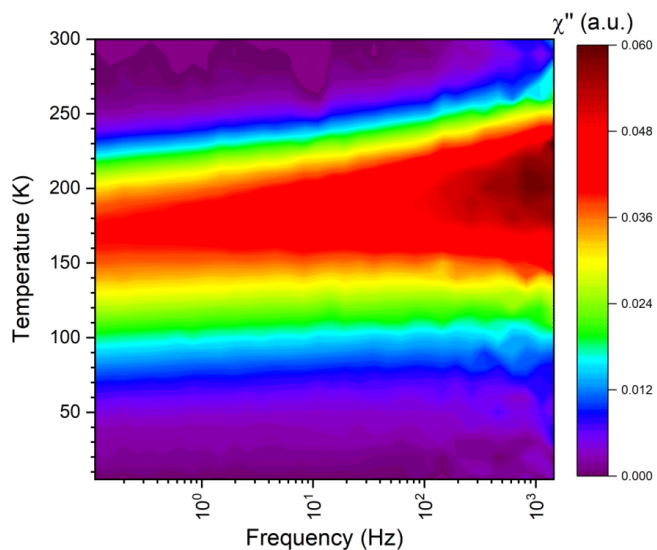
The influence of a non-magnetic surface layer on the scattering intensity is very subtle. The most sensitive to the magnetic form-factor is the 80 % nuclear-magnetic interference term. Here the deuterated solvent compensates the most of the nuclear scattering ($\Delta\text{SLD}_{\text{core}} = 1.946 \times 10^{-6} \text{ \AA}^{-2}$), however this results also in a large contrast between the solvent and the organic shell ($\Delta\text{SLD}_{\text{core}} = 4.632 \times 10^{-6} \text{ \AA}^{-2}$). Thus the organic shell thickness has to be determined very precisely before attempting to draw conclusions on the magnetic surface layer (fig. S6). For this the parallel sector is used, representing the purely nuclear scattering. A slight interaction between particles parallel to the applied field makes it necessary to include a sticky hard sphere structure factor into the fit, containing three additional fitting parameters, namely a small addition to the total particle radius (core + shell), $r1$, the volume fraction, ϕ and the stickiness, τ . Initial simulations of the influence of these parameters on the shape of the 80 % scattering curve showed that ϕ and τ have no influence on the position of the first minimum and $r1$ has a small impact, but changes the shape of the first maximum strongly, which is not observed in the data (fig. S5). Therefore, an initial value for the organic shell thickness can be obtained from the 80 % curve by only fitting the position of the first minimum without a contribution of the structure factor. This led to a value of $t_{\text{shell}} = 1.44 \text{ nm}$. After that the other contrasts were incorporated into the fit to refine the parameters of the structure factor, while at first fixing the determined shell thickness. The final step involves the refinement of the scale, $I0$, the interaction parameters and the shell thickness. The determined thickness is now 1.42 nm. With this the nuclear-magnetic interference terms can be investigated, always keeping the obtained t_{shell} and the $I0$ parameters fixed. The only parameter influencing the first peak position of the 80 % curve is now the non-magnetic surface layer thickness, h , determined to be 0.26 nm. Similar to the parallel sector analysis now the other interference terms can be included in the fit to refine the parameter for the magnetic scattering length density, which leads to $9.38 \times 10^{-7} \text{ \AA}^{-2}$. In a final step the non-magnetic surface layer thickness is refined again with all curves, giving $h = 0.28 \text{ nm}$.

References

- 1 K. Kelm and W. Mader, *Z. Naturforsch. B*, 2006, **61**, 665–671.
- 2 A. Cervellino, R. Frison, G. Cernuto, A. Guagliardi and N. Masciocchi, *J. Appl. Crystallogr.*, 2014, **47**, 1755–1761.



Supplementary Figure S6 a) Simulation of the influence of the non-magnetic surface shell thickness t_{mag} on the first peak of nuclear-magnetic interference at 80% solvent contrasts. b) Influence of the magnetic SLD. c) Influence of the organic shell thickness.



Supplementary Figure S7 Temperature/frequency mapping of the imaginary part of magnetic susceptibility. For frequencies around 10^{-2} Hz (extrapolated), corresponding to measurement times $\tau_M = 30$ s the mean relaxation frequency lies at around 160 K.